

## Article

# Experimental and Numerical Investigation of Internal Explosion in an Earth-Covered Magazine

Guangan Xu <sup>1</sup>, Yanyu Qiu <sup>1,\*</sup>, Huadao Xing <sup>2</sup>, Xiaodong Li <sup>2</sup> and Cheng Gong <sup>3</sup>

<sup>1</sup> State Key Laboratory of Disaster Prevention and Mitigation of Explosion and Impact, Army Engineering University of PLA, Nanjing 210007, China

<sup>2</sup> School of Mechanical Engineering, Nanjing University of Science and Technology, Nanjing 210094, China

<sup>3</sup> College of Civil Engineering and Mechanics, Xiangtan University, Xiangtan 411105, China

\* Correspondence: qiuyanyu78@sina.com

**Abstract:** Earth-covered magazine has some characteristics that are safer than the above-ground magazine and are more economical than underground magazine. To investigate the pressure distribution and the structural failure under the internal explosion, the scaled tests of the earth-covered magazine were conducted under a 0.5 kg TNT explosive charge. The overpressure in the 0°, 90°, and 180° directions outside the structure and the debris distribution were obtained. The numerical simulations were constructed in LS-DYNA software to analyze the test results. The results show that the external overpressure has a directional characteristic that the maximum and minimum overpressure appear in 0° and 180° directions, respectively. In the double logarithmic coordinate system, the overpressure peaks in three directions are linearly related to the scaled distance. Most of the fragments in the 0° direction hit the ground within the front range of ±60°, and the further fragments (40 m or more) were confined to a limited sector within the front range of ±30°. The internal explosion numerical simulation shows that the concrete cracks first appeared at the roof and the ground, and then the damage occurred at the intersection of the walls, and then the damage occurred at each surface. The maximum debris velocity of the side and rear walls is lower than that of the front wall due to the limitation of the soil. The motion equations of the debris combined with numerical simulation can be adopted to predict the projection distance of fragments.

**Keywords:** earth-covered magazine; internal explosion; model test; overpressure; numerical simulation; fragments distribution



**Citation:** Xu, G.; Qiu, Y.; Xing, H.; Li, X.; Gong, C. Experimental and Numerical Investigation of Internal Explosion in an Earth-Covered Magazine. *Buildings* **2022**, *12*, 1872. <https://doi.org/10.3390/buildings12111872>

Academic Editor: Fulvio Parisi

Received: 29 August 2022

Accepted: 1 November 2022

Published: 3 November 2022

**Publisher's Note:** MDPI stays neutral with regard to jurisdictional claims in published maps and institutional affiliations.



**Copyright:** © 2022 by the authors. Licensee MDPI, Basel, Switzerland. This article is an open access article distributed under the terms and conditions of the Creative Commons Attribution (CC BY) license (<https://creativecommons.org/licenses/by/4.0/>).

## 1. Introduction

An earth-covered magazine is a warehouse covered by soil on both its roof, sides, and rear [1]. Consistent with other types of magazines, such as the above-ground magazine, the earth-covered magazine is utilized to store explosives and ammunition. However, internal explosions can cause serious casualties and damage to adjacent facilities. Therefore, it is necessary to study the pressure and concrete fragments distribution law of the earth-covered magazine under the internal explosion to provide guidance for the design of weapons and ammunition storage.

The pressure generated by the internal explosion is quite different from the pressure under the air explosion, due to the existence of the structure. Compared to the free-field explosion with the characteristics of single peak value, uniform load distribution, and short-term loading, the internal explosion produces multiple peak values, uneven wall pressure distribution, and quasi-static pressure for long durations [2–6]. For example, Baker [7] obtained the internal pressure–time histories of explosives under confined blast events by experiments and found that the pressure variation showed multi-peak characteristics. Guo [8] found that the second peak pressure is about half that of the first peak pressure in a closed rectangular structure. In addition, some scholars simulated the pressure distribution

of the wall under an internal explosion through the simulation software [9–11]. The results demonstrated that the pressure is characterized by non-uniform distribution, and the pressure at the corner is the largest, followed by the peak pressure at the intersection of the surface and the surface, and the ratio of the maximum pressure peak to the minimum pressure peak is greater than 5.

Existing studies imply that the structural strength and thickness of earth covering have a significant influence on the external shock wave. Beppu [12] conducted a scaled test on the earth-covered magazine with a protective barrier in the front wall and found that the increase in the thickness of soil changes the distribution of external pressure thereon. With the increase in soil thickness, the shock wave in the rear was relatively weak. Mona [13] found that the external pressure generated by an explosion inside the earth-covered magazine was half compared to that generated by an air explosion. The United States DOD standard [14] points out that the pressure decayed by about 66.7% in an earth-covered magazine with a protective barrier, while the Chinese Standard 1 suggests that the maximum reduction in external pressure can reach 60% when protective barriers are installed in the outer space of the earth-covered magazine. Smith [15] scaled the prototype test by 1:45, and Yang [16] simulated five scaled models, both of them want to know whether meaningful results can be obtained at a small scale. It is concluded that the use of small-scale models can provide a useful method of obtaining blast-loading data for structures.

For the structural failure of an internal explosion, Wu [17] performed numerical simulations to explore the formation and projection of structural fragments under an internal explosion; they found that the number of debris increases can result in the volume of debris decrease, and the average launch velocity of debris increases when the charge mass increases; meanwhile, the fragments are distributed at all angles, but the movement directions of fragments are mainly near-perpendicular to the concrete slab. Yong [18] used a semi-theoretical method to predict the launch velocity of fragments from a concrete structure subjected to internal blast load and determined the velocity of fragments under different vented structures, which was similar to the experimental results. Pickerd [19] investigated the structural response and failure mechanism when an explosion occurred inside a closed metal container and found that quasi-static pressure is the key factor causing structural damage. Gong [20] used LS-DYNA to simulate the structural damage under explosion in a confined structure and found that a small charge promotes the formation of debris. With the increasing mass of charge, the plate failure is mainly shear stress, and then the overall failure appeared. Li [21] conducted a full-scale test on aerated masonry walls to reveal the wall response under blast loading using the equivalent degree of freedom method. The test found that the boundary conditions affect the failure mode of the walls. When the boundary was changed from that on two sides to all four sides, the failure also changed from one-way plate failure mode to two-way plate failure mode. Fang [22] used the theoretical method to estimate the dynamic response of shallow-buried box structures and determined the failure pattern of the structure under different failure conditions. Xu [23] simulated the concrete damage under different conditions and proposed a new concrete fracture criterion to predict the damage to the reinforced concrete.

In summary, many scholars have studied the internal pressure distribution generated by an internal explosion and the structure response. There are few reports on the external damage effect caused by an internal explosion of the earth-covered magazine, especially the external pressure propagation and the projection characteristics of the fragments, and the mechanism of concrete debris generation has not been clearly revealed. In the present work, an internal explosion test was conducted on the scaled model of an earth-covered magazine, and the pressure data in  $0^\circ$ ,  $90^\circ$ , and  $180^\circ$  directions and the failure mode were obtained using the pressure sensors and unmanned aerial vehicle (UAV), respectively. Meanwhile, the LS-DYNA software was employed to simulate an internal explosion within the structure. The influences of soil on the fragment projection were evaluated. The projection distance of

debris was calculated according to the motion equation. The results can provide a reference for engineering applications and damage assessment.

## 2. Experimental Set-Up

### 2.1. Apparatus

The internal explosion overpressure is mainly affected by the following parameters [16]:

1. Air: the initial pressure  $p_0$ , the air density  $\rho_a$ , the air adiabatic index  $\gamma_a$ ;
2. Explosive: the mass  $W$ , the density  $\rho_e$ , the energy released per unit mass  $e$ , the explosion product expansion index  $\gamma_e$ ;
3. Structure: the length  $l$ , the width  $b$ , the height  $h$ , the strength  $\sigma$ , Young's modulus  $E$ , the material density  $\rho_s$ ;
4. The distance from the measurement point to the explosion source  $R$ .

According to the law of similarity, the mass, length, and time dimensions M, L, and T are used as the basic dimensions, the physical dimensions of each parameter are summarized in Table 1. The functional relationship between the explosion overpressure in the structure and the influencing factors is:

$$P = f(W, p_0, \rho_a, \gamma_a, \rho_e, e, \gamma_e, l, b, h, \sigma, E, \rho_s, R) \quad (1)$$

**Table 1.** Parameters and dimensions for internal explosion.

Parameter	$P$	$t$	$W$	$p_0$	$\rho_a$	$\gamma_a$	$\rho_e$	$e$
Dimension	$ML^{-1}T^{-2}$	T	M	$ML^{-1}T^{-2}$	$ML^{-3}$	1	$ML^{-3}$	$L^2T^{-2}$
$\gamma_e$	$l$	$b$	$h$	$\sigma$	$E$	$\rho_s$	$R$	
1	L	L	L	$ML^{-1}T^{-2}$	$ML^{-1}T^{-2}$	$ML^{-3}$	L	

For the same structural material,  $E$  is not an independent factor and can be omitted, and  $\gamma_a$  and  $\gamma_e$  are dimensionless quantities and are also omitted, so Equation (1) can be simplified to Equation (2):

$$P = f(W, p_0, \rho_a, \rho_e, e, l, b, h, \sigma, \rho_s, R) \quad (2)$$

Then, taking  $W$ ,  $\rho_e$ , and  $e$  as basic quantities, Equation (2) is rewritten as:

$$\frac{P}{\rho_e e} = f \left[ \frac{p_0}{\rho_e e}, \frac{\rho_a}{\rho_e}, \frac{l}{(W/\rho_e)^{1/3}}, \frac{b}{(W/\rho_e)^{1/3}}, \frac{h}{(W/\rho_e)^{1/3}}, \frac{\sigma}{\rho_e e}, \frac{\rho_s}{\rho_e}, \frac{R}{(W/\rho_e)^{1/3}} \right] \quad (3)$$

For the same charge type under the same air conditions and the structural material remains unchanged, when  $\frac{Q_p^{1/3}}{Q_m^{1/3}} = \frac{l_p}{l_m} = \frac{b_p}{b_m} = \frac{h_p}{h_m} = \frac{R_p}{R_m} = \lambda$ ,  $P_p = P_m$ . The subscripts p and m represent the prototype and the model;  $\lambda$  is the scaling factor.

In the scaled test, the scaled model of an earth-covered magazine was used to estimate the internal explosion effect. The scaled model with the reinforced concrete structure is illustrated in Figure 1. The concrete mixture ratio was  $m_{\text{cement}}:m_{\text{water}}:m_{\text{sand}}:m_{\text{stone}} = 1:0.56:1.3:1.7$ , and the diameters of steel bars were 6 mm, 8 mm, and 10 mm, respectively, and the spacing of the reinforcement bars was 100 mm, the wall thickness was 50 mm, and a square hole with the size of 300 mm  $\times$  300 mm is set in the front wall. After 28 days of curing, the compressive strength of concrete was 34.2 MPa using a servo-hydraulic universal testing machine.

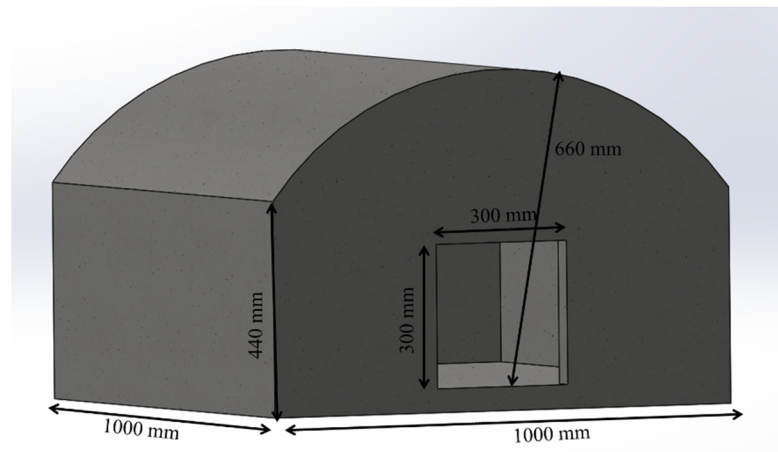


**Figure 1.** The design details of the structure.

According to the requirements in the standard [24], the scaled model of the covering soil is shown in Figure 2. The soil thickness was 70 mm, and the slope was 1:1.5.

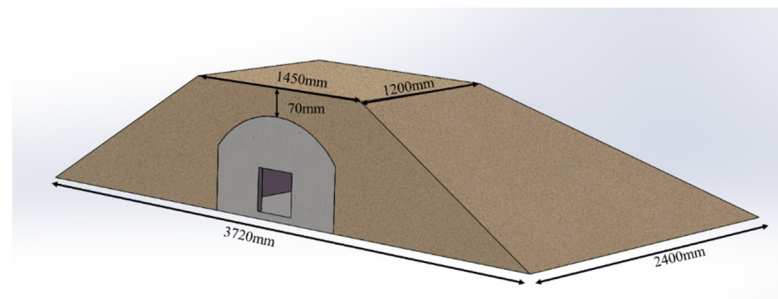


**Figure 2.** Model of covering soil.

## 2.2. Test Instruments and Equipment

Figure 3 shows the detailed sensor layout diagram: the PCB137 pressure sensors and Swiss KISTLER pressure sensors were applied in the experiment. The range of the sensor with the resonance frequency of 500 kHz was 3.45 MPa, and the signals from the pressure sensors were measured by the data acquisition instrument (DongHua 9522N, Donghua Testing Technology Co., Ltd., Taizhou, China) at a sampling rate of 1 MHz. Five sensors were arranged in the direction of  $0^\circ$ ,  $90^\circ$ , and  $180^\circ$ , respectively. The sensor bracket was fixed with the ground through the expansion bolt to avoid the brackets shaking during the test. The sensor installation is shown in Figure 4. To reduce the effect of light and heat on the pressure sensors, these sensors are coated with aluminum film and silicone grease.

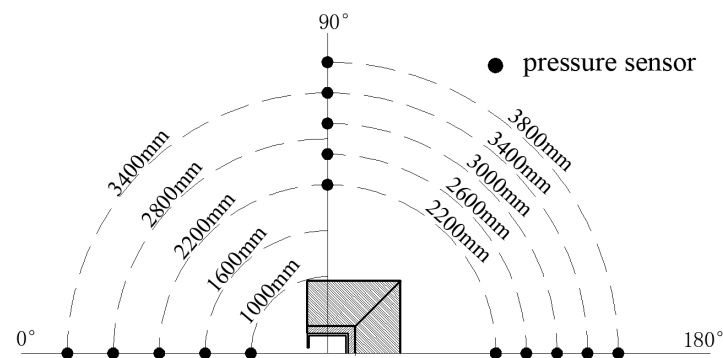


**Figure 3.** Sensor layout.



**Figure 4.** Arrangement of sensors.

A UAV was used to ascertain the overall damage before and after the test. The different surfaces were painted in different colors to distinguish the projection direction and location of the fragments after the explosion (Figure 5). After the test, the structural fragments were collected, and some debris distributions were obtained.



**Figure 5.** Surface treatment of model.

The cylindrical TNT charge was selected as the explosive, the density was set to  $1.63 \text{ g/cm}^3$ , and the total equivalent TNT mass was 0.5 kg. To enable TNT to be detonated quickly, the electric detonator was used to detonate the RDX explosive column and then detonate the TNT explosive. The explosive was fixed at the center of the model by a wooden bracket, and the axial direction of the explosive was perpendicular to the front wall. The TNT and the bracket are displayed in Figure 6.

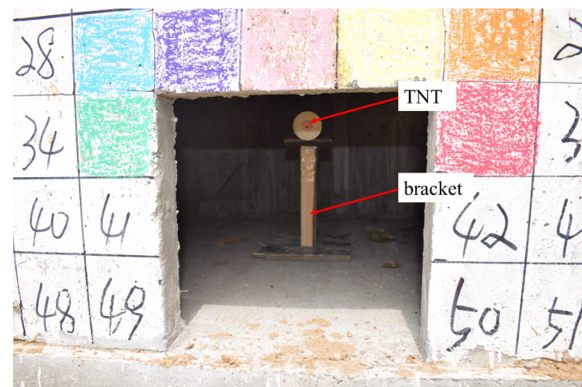


**Figure 6.** TNT and bracket.

### 2.3. Experimental Results

Figure 7 shows the typical pressure–time histories in the 0°, 90°, and 180° directions: there are multiple peaks in the pressure–time histories, which is due to the multiple reflections of the explosion shock wave within the structure. Each reflection can increase the shock wave pressure and form a new peak. Table 2 lists the overpressure peak and duration obtained by pressure sensors in three directions. The overpressure peak gradually decreases with the increase in scaled distance, and the overpressure in the 0° direction is significantly greater than that in the 90° and 180° directions. The peak overpressure in the 180° direction is the smallest. This finding indicates that the external overpressure caused by the internal explosion of an earth-covered magazine presents clear directionality. This is because there is a hole in the front wall (0° direction). Before the structural failure, the shock wave can only be released from the hole, which makes the shock wave converge at the front hole and increases the peak overpressure in the 0° direction. The shock waves in the 90° and 180° directions are composed of two parts, some waves diffracted from the front wall, and others were released from other walls after the structural failure. Due to the rapid attenuation of the shock wave, and the energy dissipation on the structure wall, the overpressure in the 90° and 180° directions is small. However, the duration of positive pressure is the longest and the shortest in 180° direction and 0° direction, respectively. This is due to the superposition of multiple shock waves in the 180° direction, leading to a long duration of overpressure.

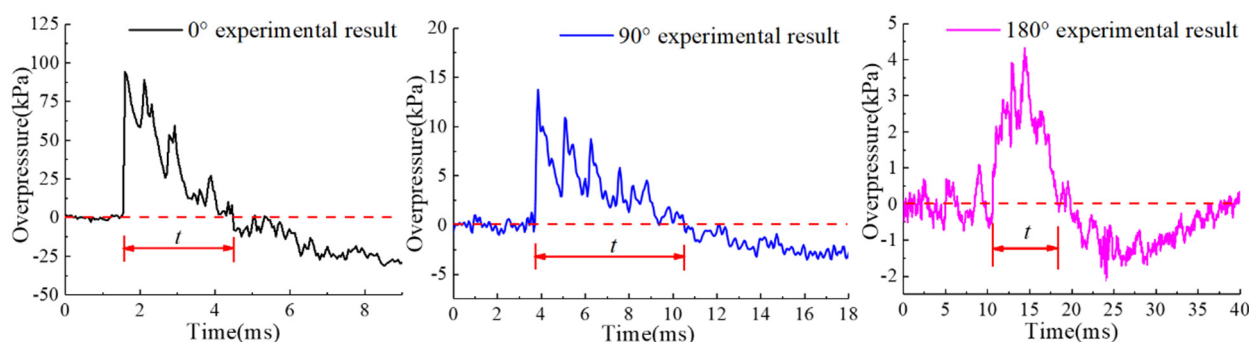


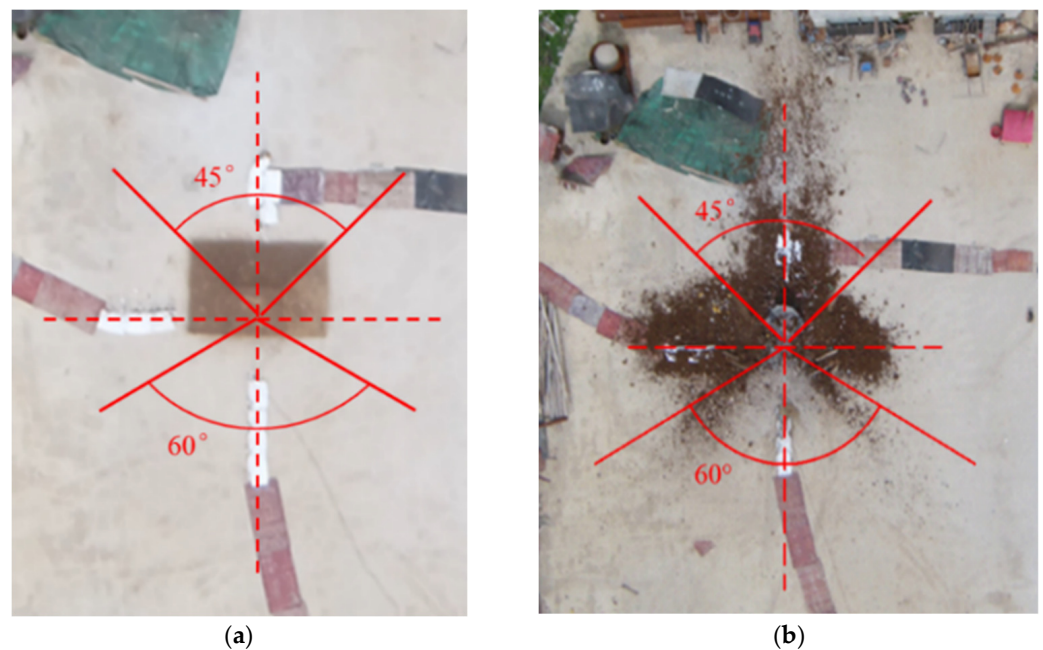
Figure 7. Typical pressure-time histories in different directions.

Table 2. Pressure parameters.

Sensor Number	Range (m)	Scaled Distance (m/kg <sup>1/3</sup> )	Overpressure (kPa)	Duration of Positive Pressure (ms)	
0°	1	1.114	307.23	1.22	
	2	1.728	212.41	2.61	
	3	2.331	–	–	
	4	2.931	101.2	2.87	
	5	3.551	4.474	71.53	2.96
90°	6	2.315	18.29	6.97	
	7	2.705	16.76	6.92	
	8	3.115	3.925	–	–
	9	3.505	4.416	15.39	7.05
	10	3.910	4.926	13.74	7.11
180°	11	2.315	6.3	9.18	
	12	2.705	5.53	10.15	
	13	3.115	3.925	–	–
	14	3.505	4.416	–	–
	15	3.910	4.926	4.6	9.41

Note: Sensors 3, 8, 13, and 14 were damaged by the fragments, and test data were not attained.

Figure 8 shows the photographs of the model before and after the explosion obtained by the UAV. It can be found that the outer space of the earth-covered magazine is divided into four regions according to the dispersion of soil, namely the front ( $-60^\circ$  to  $60^\circ$ ), the rear ( $135^\circ$  to  $225^\circ$ ), and the sides ( $60^\circ$  to  $135^\circ$ ,  $225^\circ$  to  $300^\circ$ ), which are consistent with the division of the outer region of the earth-covered magazine given in the specification. Figure 9 depicts the model after the destruction of the earth-covered magazine: the debris projection distance in the directions of the two sidewalls and the rear wall is small, mostly falling within the range of 5 m around the model, and the projection distance of the soil in the directions of the two sidewalls is not more than 5 m. However, due to the damage to the roof under the shock wave (Figure 9), the soil above flies backward, and the furthest projection distance of the soil in the  $180^\circ$  direction is more than 10 m. The debris projection distance of the front wall is much larger than that of the other walls due to the absence of the constraining effect of the soil thereon. As shown in Figure 10, the debris projection distance in the direction of the front wall reaches 82 m, and the debris is distributed in the range of  $\pm 60^\circ$  in the direction of the front wall. The further fragments (40 m or more) were confined to a limited sector within the front range of  $\pm 30^\circ$ .



**Figure 8.** Comparison of models before and after the explosion. (a) Before; (b) after.



**Figure 9.** Model failure. (a) Left view; (b) right view.

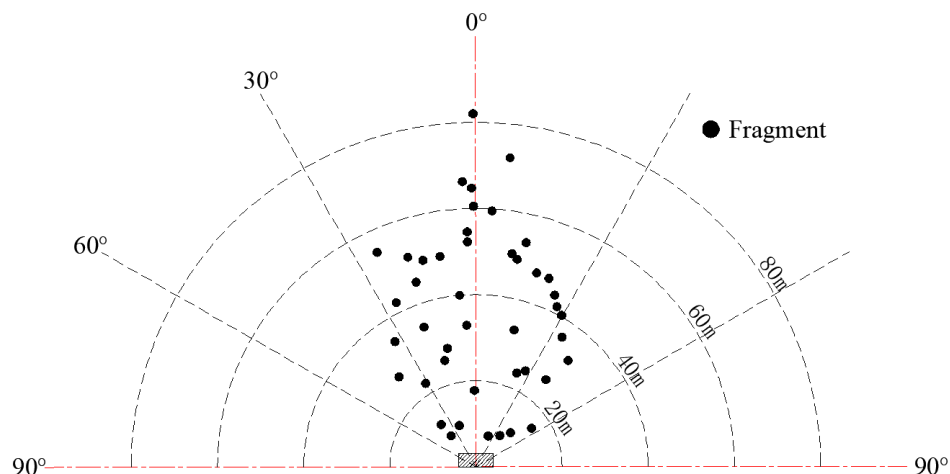


Figure 10. Distribution of structural fragments.

### 3. Discussion

#### 3.1. Pressure Curve Analysis

According to the fitting formula of the external overpressure peak value of the explosion inside the earth-covered magazine in Kim [25], the scatter plot between P-z in three directions was obtained according to the experimental data (Figure 11): there is a quasi-linear relationship between the peak overpressure and the scaled distance in double logarithmic coordinates, and Equation (4) represents the best fits to the data. With the increase in scaled distance, the peak overpressure values attenuate continuously. The peak pressure in the 0° direction decays faster than that in 90° and 180° directions, and the peak overpressure in the 0° direction is larger than that in other directions.

$$\begin{aligned}
 0^\circ : P &= 10^{(2.545 - 0.194 \lg(z) - 1.333 \lg^2(z))} \\
 90^\circ : P &= 10^{(1.299 + 0.188 \lg(z) - 0.592 \lg^2(z))} \\
 180^\circ : P &= 10^{(1.132 - 0.822 \lg(z) + 0.202 \lg^2(z))}
 \end{aligned}
 \tag{4}$$

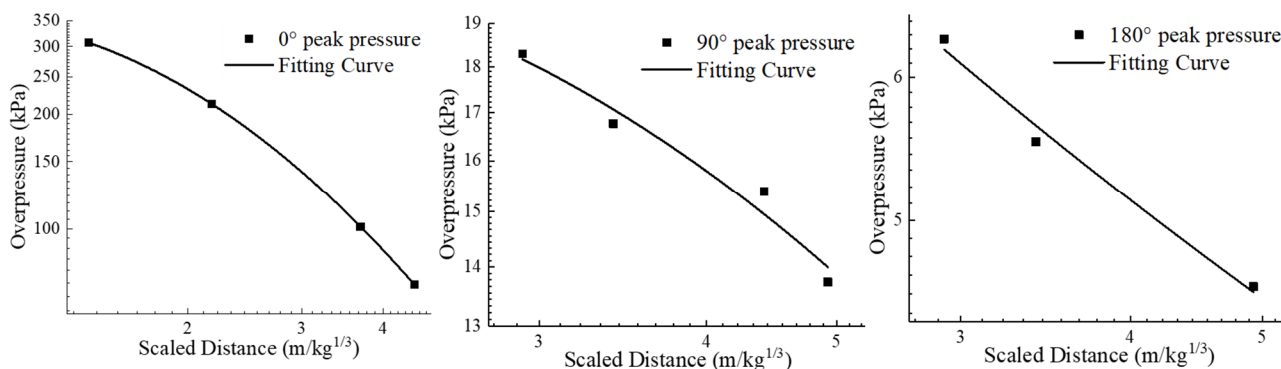


Figure 11. P-z fitting curves in different directions.

#### 3.2. Comparative Analysis of Air Explosion and Implosion of Earth-Covered Magazine

Table 3 lists the test results and the calculation results of the peak overpressure formula of ground explosion air 7. The overpressure caused by the air explosion is given by Equation (5).

$$\begin{cases}
 P = \frac{2.006}{z} + \frac{0.194}{z^2} - \frac{0.004}{z^3}, & 0.05 \leq z \leq 0.5 \\
 P = \frac{0.067}{z} + \frac{0.301}{z^2} + \frac{0.431}{z^3}, & 0.5 \leq z \leq 70.9
 \end{cases}
 \tag{5}$$

where P represents the peak overpressure; z is the scaled distance,  $z = R/W^{1/3}$ ; R is the distance between the measuring point and the explosion center; W denotes the mass of TNT.

Table 3. Model for overpressure reduction.

Position	Range (m)	Scaled Distance (m/kg <sup>1/3</sup> )	Peak Pressure $P_1$ /kPa	Peak Pressure $P_2$ /kPa	Reduction $\xi$ /%
0°	1.114	1.404	307.23	356.41	13.80
	1.728	2.177	212.41	136.04	−56.14
	2.331	2.937	114.79	74.73	−53.61
	2.931	3.693	101.2	48.77	−107.50
	3.551	4.474	71.53	34.83	−105.37
90°	2.315	2.917	18.29	75.72	75.85
	2.705	3.408	16.76	56.46	70.32
	3.115	3.925	15.94	43.74	63.56
	3.505	4.416	15.39	35.61	56.78
	3.910	4.926	13.74	29.61	53.60
180°	2.315	2.917	6.3	75.72	91.68
	2.705	3.408	5.53	56.46	90.21
	3.115	3.925	5.18	43.74	88.16
	3.505	4.416	4.84	35.61	86.41
	3.910	4.926	4.60	29.61	84.46

Note,  $P_1$  was the experimental data, other data were calculated by way of the fitting formulae,  $P_2$  was calculated according to Equation (5),  $\xi = (P_2 - P_1)/P_2$ .

Table 3 shows that in the 0° direction, the peak overpressure  $P_1$  in the near-field area is smaller than that of  $P_2$  at the same scaled distance, while the peak overpressure results in the far-field area are opposite. The overpressure peaks  $P_1$  in the 90° and 180° directions are always smaller than the air explosion overpressure  $P_2$ . Compared with the air explosion with the same overpressure peak in each direction, the overpressure peak value of the internal explosion in the 0° direction is larger than that of the air explosion at the same scaled distance, while the overpressure peak value in other directions is smaller than that of the air explosion. Indicating that the overpressure propagation with an earth-covered magazine demonstrates obvious directionality.

#### 4. Numerical Simulations

Numerical simulations were mainly aimed at assessing the influences of explosion in the earth-covered magazine on the propagation of shock waves and structural failure. LS-DYNA finite element software was adopted to calculate and the fluid–structure coupling algorithm was employed to obtain the pressure time histories at different locations and the failure modes of the structure upon an internal explosion.

##### 4.1. Finite Element Model

The model is a symmetric structure, and a half-model was established for the convenience of calculation. The models of air, explosives, concrete structure, steel bar, and soil were built in the software. For air, explosives, and concrete, eight-node solid elements were used, for steel bars, a two-node beam element was used. The element adopted the ALE multi-material algorithm, in which the air and explosives adopted the ALE mesh, the concrete element used the Lagrangian mesh, and the structure and air and explosives were subject to a penalty coupling function in the fluid–structure interaction algorithm. The fluid–structure interaction algorithm was also used between concrete and steel bars (Figure 12). To replicate the throwing of soil, the soil was calculated in the form of the smoothed particle hydrodynamics (SPH). Except for the symmetry plane and the ground, non-reflection boundaries are set at other air boundaries, the earth-covered magazine model is only limited to the vertical displacement of the bottom surface, the symmetry boundary was set at the symmetry plane, and automatic\_node\_to\_surface is set between the soil and the structure. The keyword LOAD\_BODY\_Z was adopted to simulate the influence of gravity.

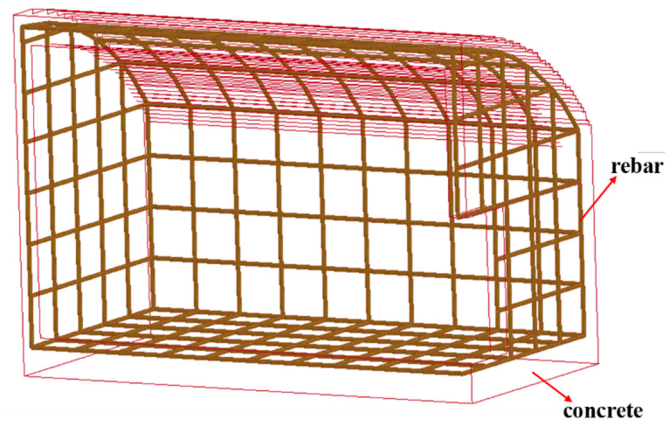


Figure 12. Model of the structure.

To verify the grid convergence, four element sizes of 8 mm, 10 mm, 15 mm, and 20 mm were selected for the concrete model. The element size of the soil around the structure was the same as that of the concrete element, and the size of the soil on the slope was twice that of the concrete element. Figure 13 shows the fragment velocities of different walls under different concrete element sizes. It can be seen from the figure that as the element size decreases, the wall fragment velocities increase continuously. However, when the element size is less than 10 mm, the change in fragment velocity is small, so the structural element size is set to be 10 mm and the steel element size is 5 mm; the model of the earth-covered magazine is shown in Figure 14.

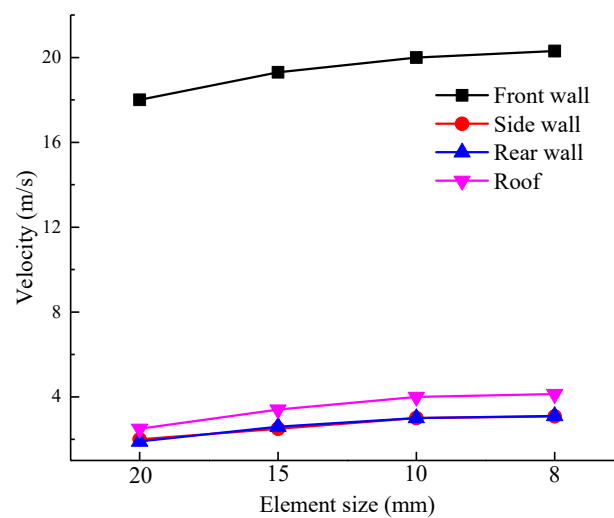


Figure 13. The effect of mesh size.

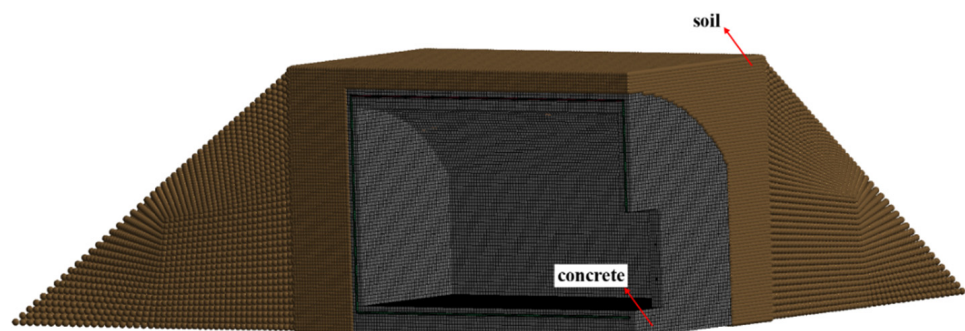
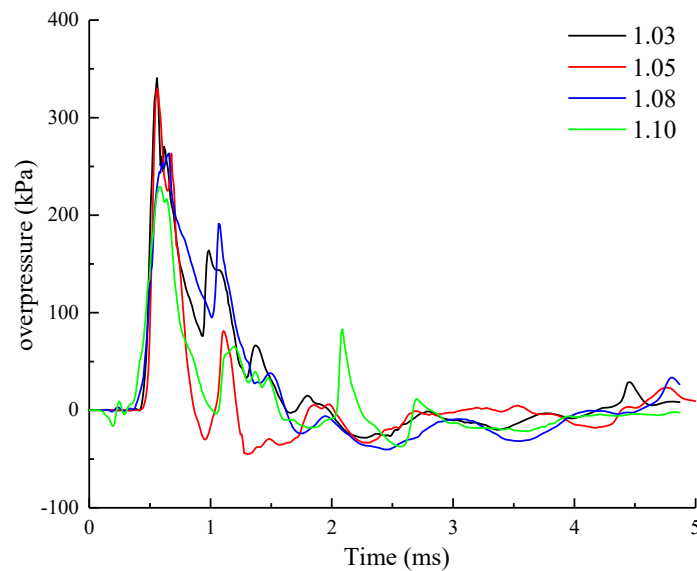


Figure 14. Earth-covered magazine model.

The air was meshed with a gradient mesh to reduce the number of elements, thereby decreasing the calculation time. To study the influence of mesh refinement on the results, four mesh densities of 1.1, 1.08, 1.05, and 1.03 were used for mesh convergence analysis. The pressure curve at the same position is displayed in Figure 15. The basic information about each of the pressure–time histories is summarized in Table 4.



**Figure 15.** The effect of mesh refinement.

**Table 4.** Details of pressure–time histories.

Mesh Density	Peak Pressure/kPa	Difference/%
1.03	340.63	-
1.05	330.19	−3.06
1.08	263.43	−22.66
1.10	228.93	−32.79

Note: the difference is expressed as the rate of change in the overpressure peak value under different mesh densities to the overpressure peak at a mesh density of 1.03.

The results show that as the mesh refinement decreases (from 1.05 to 1.10), the overpressure peak increases gradually. When the rate of change thereof is adjusted from 1.05 to 1.03, the pressure peak does not increase significantly, while the number of elements increases from 401,940 to 805,752. In contrast, it is more appropriate to use a mesh gradient of 1.05. The model is shown in Figure 16.

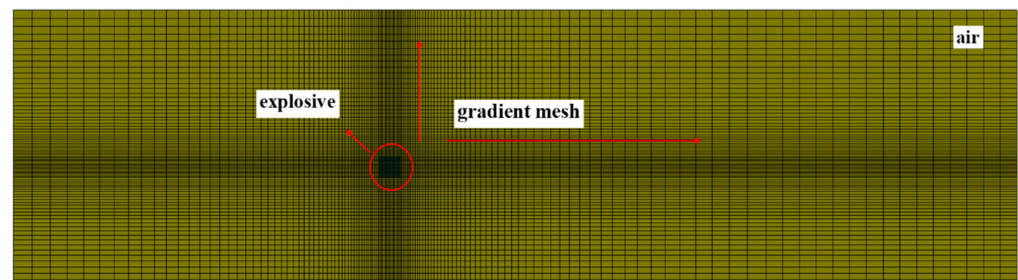


**Figure 16.** Model of air and explosive.

#### 4.2. Material Properties

Air is described using the \*MAT\_NULL material model and the EOS\_LINEAR\_POLYNOMIAL polynomial equation of state 26, where the equation of state is expressed as:

$$P = C_0 + C_1\mu + C_2\mu^2 + C_3\mu^3 + (C_4 + C_5\mu + C_6\mu^2)E \quad (6)$$

$$\mu = \frac{1}{V_1} - 1 \quad (7)$$

where  $P$  is the gas pressure,  $C_0$ – $C_6$  are state parameters, where  $C_0 = C_1 = C_2 = C_3 = C_6 = 0$ ,  $C_4 = C_5 = 0.4$ ;  $E_1$  is the internal energy of the gas, taking  $2.5 \times 10^5$  J here,  $V_1$  is the relative volume, taken as 1.0.

The explosive is described using the \*MAT\_HIGH\_EXPLOSIVE\_BURN material model and the EOS\_JWL polynomial equation of state [26], where the equation of state is expressed as:

$$P = A \left(1 - \frac{\omega}{R_1 V}\right) e^{-R_1 V} + B \left(1 - \frac{\omega}{R_2 V}\right) e^{-R_2 V} + \frac{\omega E}{V} P = A \left(1 - \frac{\omega}{R_1 V}\right) \quad (8)$$

where  $P$  is the pressure;  $A$ ,  $B$ ,  $R_1$ , and  $R_2$  are the material parameters, whose values are  $3.712 \times 10^{11}$ ,  $3.23 \times 10^9$ , 4.15, and 0.95, respectively;  $E$  is the internal energy per unit volume, which is  $7 \times 10^9$ ;  $V$  denotes the relative volume, taken as 1.0.

The concrete adopts the \*MAT\_JOHNSON\_HOLMQUIST\_CONCRETE model [26], which is suitable for concrete materials with large strain, high strain rate, and high stress, and considers the effect of equivalent strength due to damage accumulation. Its material constitutive equation is:

$$\sigma^* = [A(1 - D) + BP^{*N}] (1 + C \ln \dot{\epsilon}^*) \quad (9)$$

where  $\sigma^*$  is the normalized equivalent stress,  $P^*$  is the normalized hydrostatic pressure,  $\dot{\epsilon}^*$  is the strain rate,  $A$ ,  $B$ ,  $N$ , and  $C$  denote the normalized cohesive strength, pressure hardening coefficient, pressure hardening index, and strain rate hardening coefficient, respectively;  $D$  is the degree of damage degree, as given by:

$$D = \sum \frac{\Delta \epsilon_p + \Delta \mu_p}{D_1 (P^* + T^*)^{D_2}} \quad (10)$$

where  $\Delta \epsilon_p$  and  $\Delta \mu_p$  are the increments of the equivalent plastic strain and equivalent volumetric strain within the unit during a single cycle calculation;  $P^*$  is the normalized pressure;  $T^*$  is the normalized maximum tensile hydrostatic pressure;  $D_1$  and  $D_2$  are the material damage coefficients, and the selected material parameters are listed in Table 5. The failure mode of concrete is the maximum strain failure, the maximum strain failure is 0.0015.

**Table 5.** Parameters used to model concrete.

Parameter	Density	A	B	N	C	$f_c$
Value	2300	0.79	1.60	0.61	0.007	34.2
$S_{\max}$	Shear modulus	$D_1$	$D_2$	$\epsilon f_{\min}$	$p_c/\text{MPa}$	$\mu_c$
7.0	12.5	0.05	1.0	0.01	15.0	0.0001
$K_1/\text{GPa}$	$K_2/\text{GPa}$	$K_3/\text{GPa}$	$P_1/\text{GPa}$	$\mu_1$		
85.0	−171.0	208.0	0.85	0.10		

The rebar adopts the \*MAT\_PIECEWISE\_LINEAR\_PLASTICITY material model [26] and considers the influence of the strain rate on the material strength. The dynamic influence coefficient  $\psi$  of the strain rate on the strength is obtained as follows:

$$\Psi = 1 + \left( \frac{\dot{\epsilon}}{C} \right)^P \quad (11)$$

where  $\dot{\epsilon}$  is the material strain rate;  $C$  and  $P$  are coefficients influencing strengths, their values are  $10^{-4}$  and 0.009, respectively.

The earth cover adopts the \*MAT\_SOIL\_AND\_FOAM model, which is suitable for the calculation of soil and foam. Since the earth cover is a loose medium, it will disperse in the air when subjected to small disturbances. Therefore, when inputting parameters, the influence of the plastic factor of the material is not considered, and its material is constitutively modeled as follows [26]:

$$\phi = J_2 - [a_0 + a_1 p + a_2 p^2] \quad (12)$$

where  $\phi$  represents the partial ideal plastic yield function,  $J_2$  is the second stress invariant,  $J_2 = \frac{1}{2} s_{ij} s_{ij}$ ,  $s_{ij}$  is the deviatoric stress tensor, and on the yield surface  $J_2 = \frac{1}{3} \sigma_y^2$ ,  $\sigma_y$  is the uniaxial yield stress;  $a_0$ ,  $a_1$ , and  $a_2$  are constants;  $p$  is the pressure.

When the yield strength of the material is not considered,  $\phi = 0$ .

$$a_0 = \frac{1}{3} \sigma_y^2, \quad a_1 = 0, \quad a_2 = 0.$$

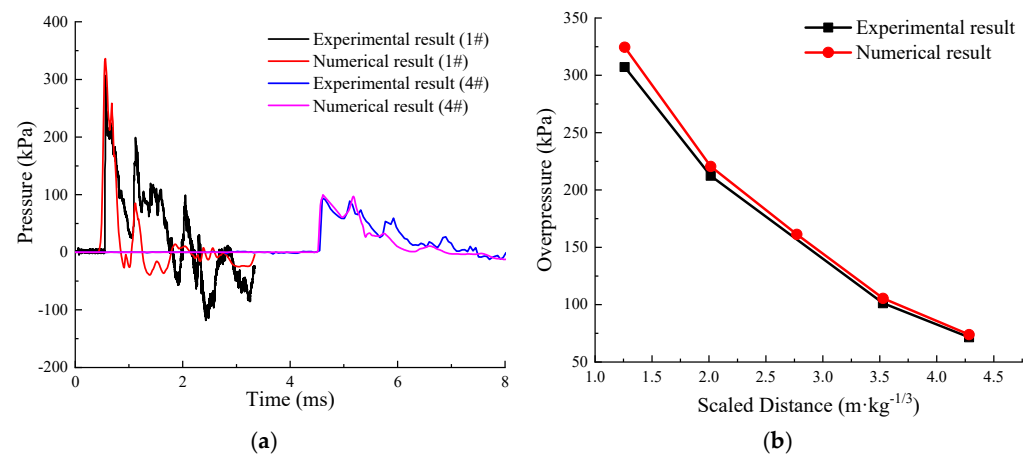
Its material parameters are summarized in Table 6.

**Table 6.** Material parameters of the soil [27].

Parameter	Density (kg/m <sup>3</sup> )	Shear Modulus (Pa)	Bulk Modulus (Pa)	PC (Pa)
Value	1800	$63.9 \times 10^6$	$3 \times 10^{10}$	0
EPS1	EPS2	EPS3	EPS4	EPS5
0.0	-0.1	-0.161	-0.192	-0.224
EPS6	EPS7	EPS8	EPS9	EPS10
-0.246	-0.271	-0.283	-0.29	-0.40
P1 (Pa)	P2 (Pa)	P3 (Pa)	P4 (Pa)	P5 (Pa)
0.0	$2.0 \times 10^7$	$4.0 \times 10^7$	$6.0 \times 10^7$	$1.2 \times 10^8$
P6 (Pa)	P7 (Pa)	P8 (Pa)	P9 (Pa)	P10 (Pa)
$2.0 \times 10^8$	$4.0 \times 10^8$	$6.0 \times 10^8$	$8.0 \times 10^8$	$4.1 \times 10^9$

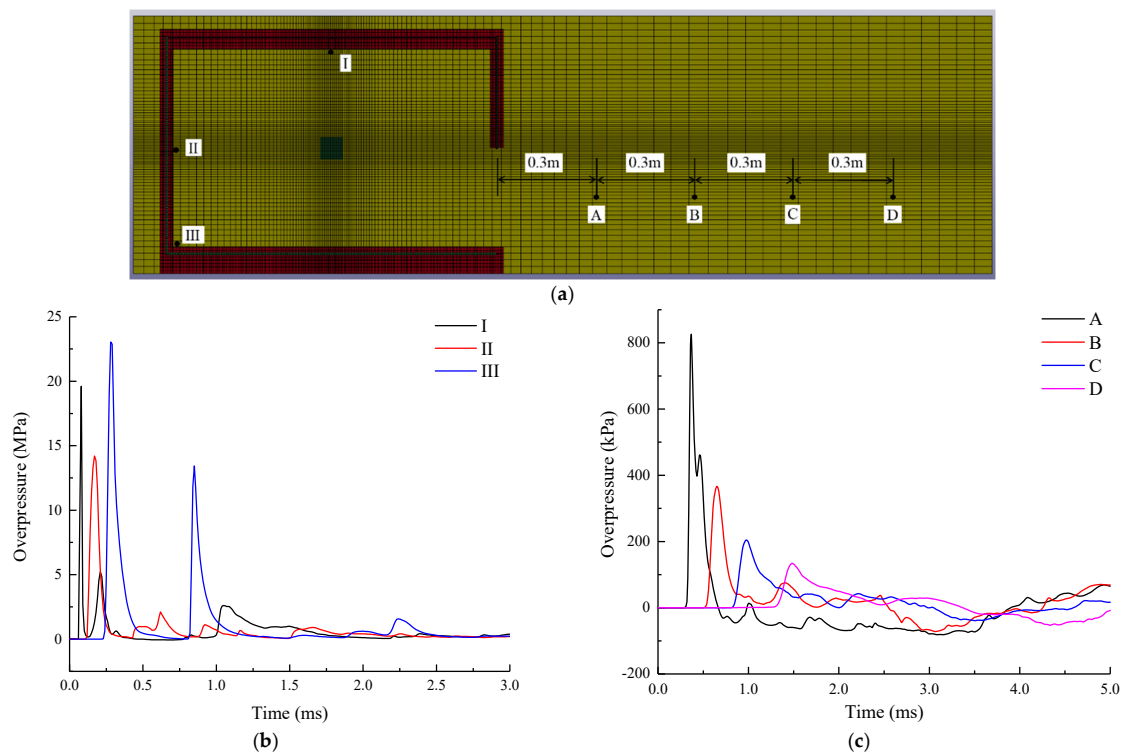
#### 4.3. Numerical Results

Figure 17a shows the comparison of pressure between the test results and the simulation results at the 1# and 4# gauges in the 0° direction. The first peak overpressure measured by the test is 306.75 kPa and 101.2 kPa, respectively, and the peak overpressure obtained by simulation is 324.51 kPa and 105.43 kPa (a difference of 5.79% and 4.15%), respectively. Figure 17b represents the comparison of the overpressure peak between the experimental result and numerical result, overpressure from the tests and simulations are in reasonable agreement. The numerical simulation is the result under ideal working conditions, and the test process is affected by environmental conditions, which is the reason for the low peak overpressure. This finding shows that the model and related parameters selected by numerical simulation match the prevailing test conditions.



**Figure 17.** Comparison of experiment and numerical simulation. (a) Comparison of overpressure time-history curves of 1# and 4# gauge; (b) comparison of overpressure peak in the  $0^\circ$  direction.

Figure 18 shows the pressure time histories at different positions obtained from the simulation, in which Figure 18a depicts the measuring point positions, and Figure 18b displays the pressure time histories at different positions inside the structure. The three positions are the blasting center at the projection of the roof, the blasting center at the projection of the rear wall, and the intersection of the rear wall and the ground. It can be seen from the figure that the peak overpressure at the corner point is higher than the pressure elsewhere, which matches the results of Edri 2. Since the waves converge at the internal edge line and corner point of the structure, the pressure at these positions increases. Figure 18c illustrates the pressure time histories at different locations in the external space. The peak overpressure value is decreasing with the increase in scaled distance, while the duration of positive pressure increases with the increase in scaled distance.



**Figure 18.** Pressure-time histories at different locations; (a) location of measuring points; (b) internal; (c) external.

Figures 19 and 20 show the propagation of shock waves in the structure and the destruction process of the structure, respectively. Combining Figures 19 and 20, it can be found that since the roof and ground are close to the center of the explosion, the shock wave can reach the roof and ground in only 0.09 ms. Due to the long distance between explosives and walls, including the front wall, the side wall, and the rear wall, the arrival time is a little later, about 0.13 ms. When the time reaches 0.20 ms, the shock wave begins to vent from the front wall. The structure starts to fail from 0.13 ms, and the damaged area first occurs on the roof and ground, which is consistent with the results obtained by Mona [13]. Under the internal explosion in the earth-covered magazine, the roof first begins failure. The cracks at the intersection of the walls begin to develop when the time reaches 0.16 ms. When the time reaches 0.48 ms, the cracks at the intersection are basically connected, and there are multiple cracks in the 45° direction on the side wall and the rear wall. When the time reaches about 1.2 ms, all the walls are damaged severely, and each wall is separated. The failure phenomena of the model are shown in Figure 21. It can be seen from the figure that each wall is severely damaged under the impact of the blast shock wave, resulting in many fragments. The debris in the front wall has a long launch distance, which can be clearly observed, while the debris generated by the side wall and the rear wall is affected by the soil, so the launch distance is limited. Soil has a certain effect on the failure of the model.

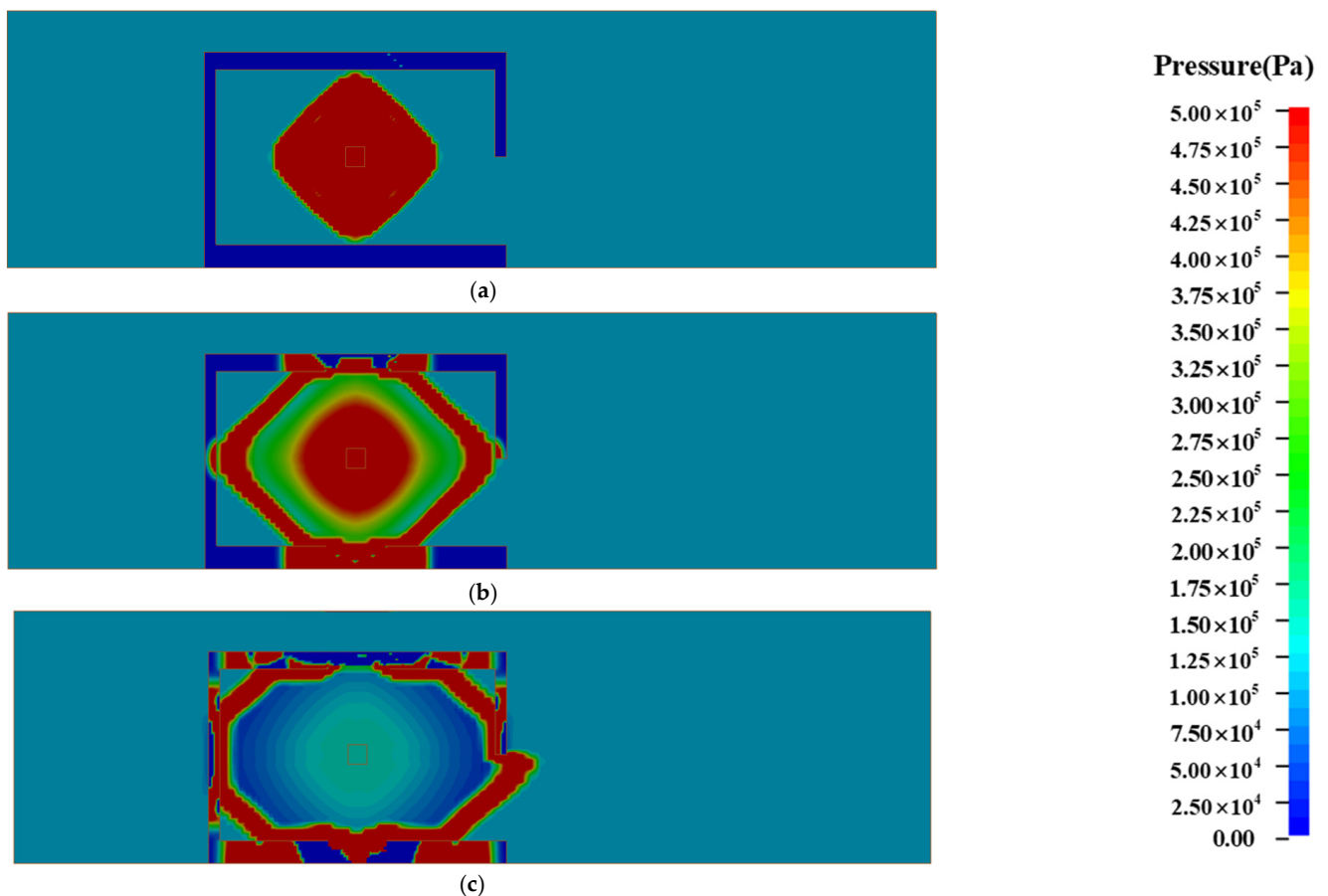


Figure 19. Shock wave propagation. (a) 0.09 ms; (b) 0.13 ms; (c) 0.20 ms.

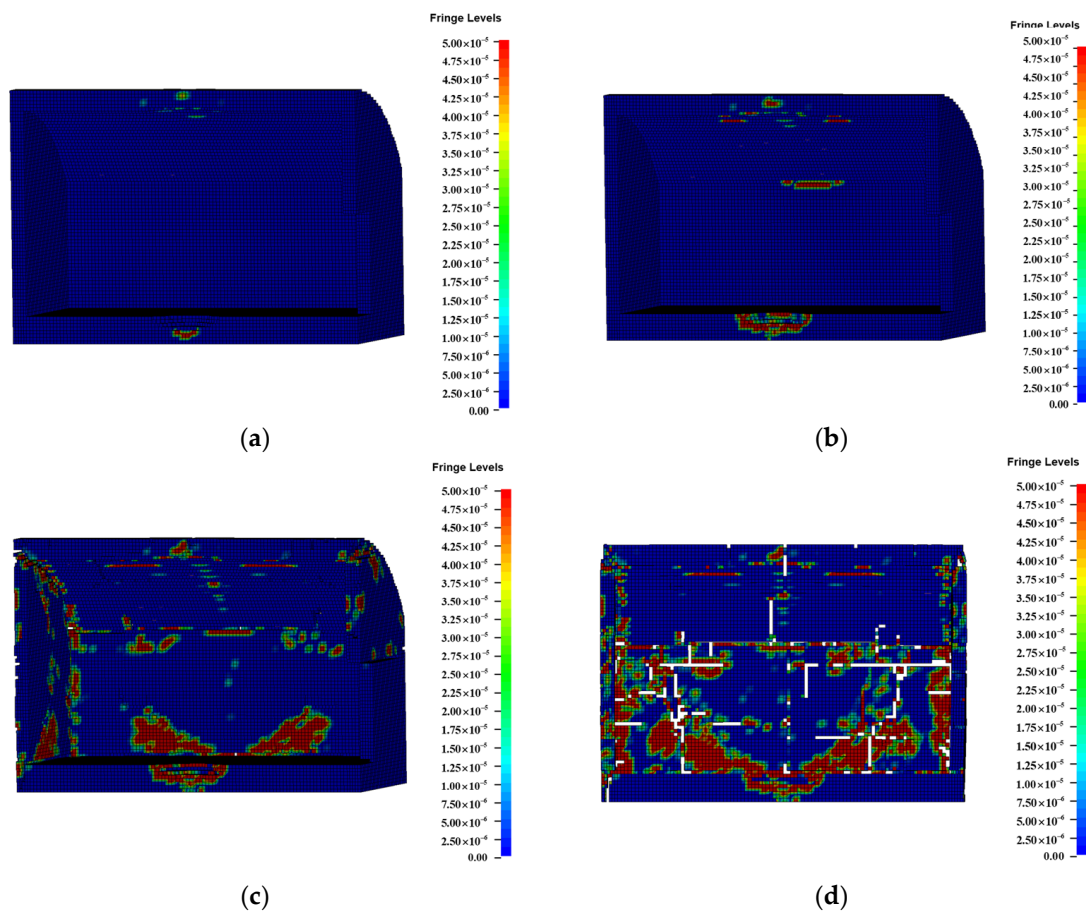


Figure 20. Structural crack development. (a) 0.13 ms; (b) 0.16 ms; (c) 0.48 ms; (d) 1.2 ms.

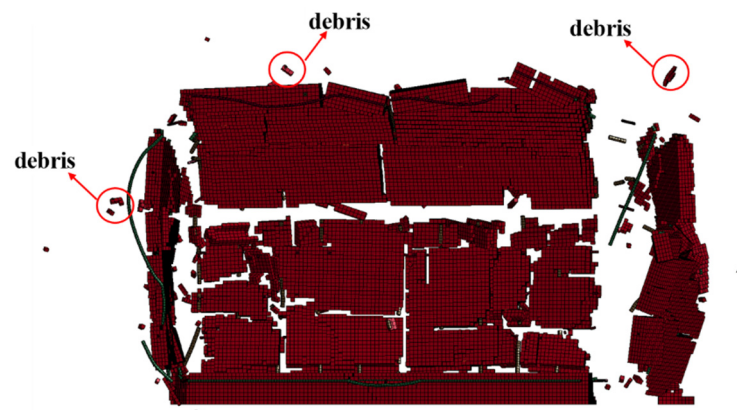


Figure 21. Model failure form.

## 5. Fragment Projection Distance

Under the action of an internal explosion, the structure of the earth-covered magazine produces countless fragments, and the fragments launch outward under the impetus of the shock wave. The launching process is subject to the interaction of air and gravity, and the calculation is more complex. Scholars have studied the equations of motion and trajectory of fragments under various explosions [28–30]. The equation of motion of fragments in the air can generally be calculated by the following formulae (divided mainly into three parts: horizontal motion, ascending motion, then descending motion).

Horizontal

$$\begin{aligned} \dot{x}(t) &= \frac{u \cos(\varphi)}{1+ktu \cos(\varphi)} \\ x(t) &= \frac{1}{k} \ln[1 + ktu \cos(\varphi)] \end{aligned} \tag{13}$$

Ascent

$$\begin{aligned} \dot{y}(t) &= \frac{\tan(\beta-\alpha gt)}{\alpha} \\ y(t) &= -\frac{1}{2} \left\{ \frac{\ln[1+\tan^2(\frac{-\beta+\alpha gt}{\alpha})]}{\alpha^2 g} \right\} + \frac{1}{2} \left\{ \frac{\ln[1+\tan^2(-\beta)]}{\alpha^2 g} \right\} \end{aligned} \tag{14}$$

Decent

$$\begin{aligned} \dot{y}(t) &= \frac{1-\exp(\zeta t-2\beta)}{\alpha[1+\exp(\zeta t-2\beta)]} \\ y(t) &= -\frac{\ln\langle 1+\exp\{\frac{2kt}{\alpha}-2\arctan[\alpha u \sin(\varphi)]\}\rangle}{k} + \frac{\ln\langle \exp\{\frac{2kt}{\alpha}-2\arctan[\alpha u \sin(\varphi)]\}\rangle}{2k} \\ &+ \frac{\ln\langle 1+\exp\{-2\arctan[\alpha u \sin(\varphi)]\}\rangle}{k} - \frac{\ln\langle \exp\{-2\arctan[\alpha u \sin(\varphi)]\}\rangle}{2k} \end{aligned} \tag{15}$$

where  $u$  is the fragment launch velocity,  $k$  represents the drag factor,  $k = \frac{\rho C_D A_D}{2M}$ ,  $\rho$  is the density of the air,  $C_D$  refers to the drag coefficient,  $A_D$  is the drag area,  $M$  is the mass of the debris fragment;  $\alpha = \sqrt{\frac{k}{g}}$ ,  $\beta = \arctan[\alpha u \sin(\varphi)]$ ,  $\zeta = \frac{2k}{\alpha}$  refers to coefficients,  $g$  is the acceleration of gravity, and  $\varphi$  is the fragment orientation.

Figure 22 presents the summary of the velocity of concrete elements in each region by numerical simulations. The time sequence of velocity mutation is the same as that of the shock wave arrival. The first impact is on the roof, followed by that on the walls. The front wall has a relatively large launch velocity, which can reach 25 m/s due to the absence of any constraining effect from the soil. The velocities of the roof, sidewall, and rear wall increase continuously under the action of the blast shock wave, however, due to the influence of the soil, there is a maximum velocity observed thereat, around 10 m/s. After passing the value, the velocity gradually decreases, and the launch velocity of the fragment is only 4 m/s.

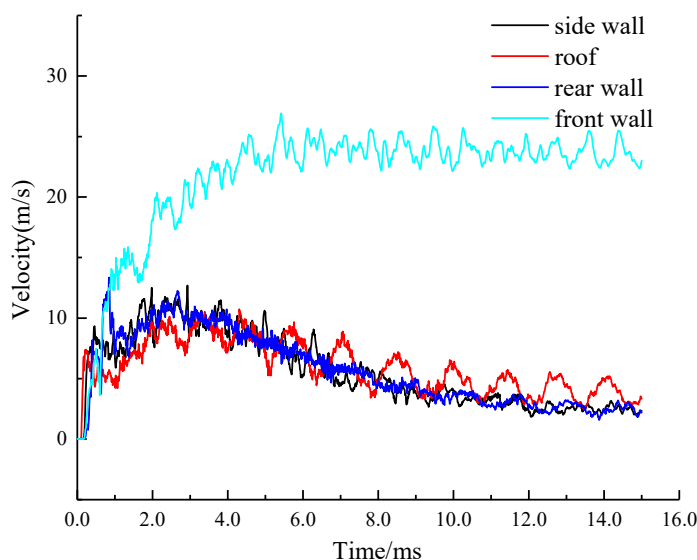


Figure 22. Launch velocity of concrete fragments.

There is soil in the sidewalls, rear wall, and roof of the earth-covered magazine, so only the projection distance of debris in the front wall direction was investigated here.

As shown in Figure 22, the maximum fragment velocity of the front wall reaches 25 m/s. For the drag coefficient  $C_D$ , it is generally considered that the cylindrical shape

is scattered, and the values lie between 0.8 and 1.1. For the plane shape, the values lie between 1.1 and 1.8 [31], and the acceleration of gravity  $g$  is  $9.8 \text{ m/s}^2$ .

Due to the explosion inside the earth-covered magazine, countless fragments with various shapes were produced, and the shapes of the heavier structural debris (20 g or more) were mainly columnar. Figure 23 shows the four concrete fragments. The original position can be found according to their color. The projection of fragments obtained by numerical simulation was compared with the actual projection distance of fragments, as shown in Table 7. The results show that the projection distance of fragments could be predicted by using numerical simulation and equations of fragment motion, so a more reliable safe distance could be obtained.

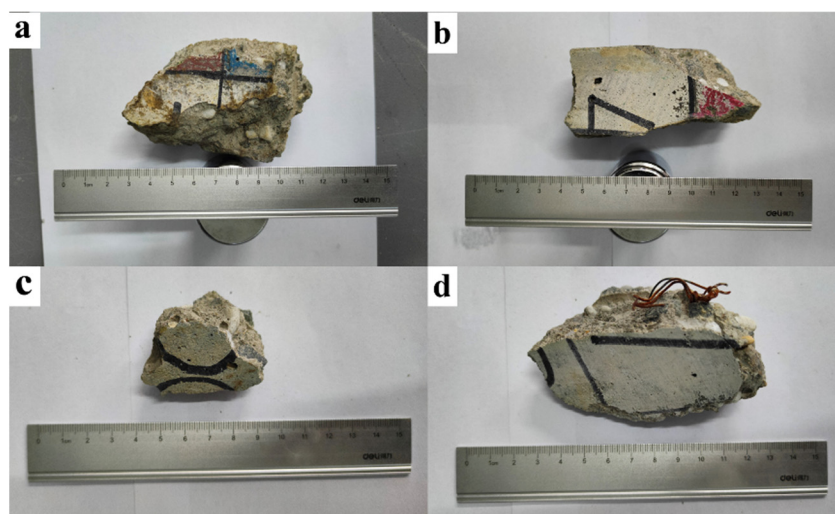


**Figure 23.** Concrete fragments and the size. (a) fragment a; (b) fragment b; (c) fragment c; (d) fragment d.

**Table 7.** Comparison of actual projection distance and calculated distance.

	Fragment Mass (kg)	Projection Distance (m)		Difference (%)
		Model Test	Simulation	
a	0.4049	43.85	45.81	4.47
b	0.3358	64.76	60.42	6.70
c	0.0479	82.01	80.48	1.86
d	0.1634	50.17	52.49	2.08

## 6. Conclusions

The internal explosion test was conducted on the scaled model of the earth-covered magazine, and the external pressure distribution and the failure mode of the model were determined. LS-DYNA software was used to simulate the explosion in the earth-covered magazine, and to study the variation and distribution of pressure and fragments, and the following conclusions were obtained:

- (1) The external pressure of the earth-covered magazine explosion shows obvious directionality, that the peak overpressure in the  $0^\circ$  direction is the largest, followed by those in the  $90^\circ$  and  $180^\circ$  directions. The external pressure–time histories have multiple peaks, and the positive pressure duration in  $90^\circ$  and  $180^\circ$  directions is significantly longer than that in the  $0^\circ$  direction.
- (2) The relationship between the peak overpressure and the scaled distance is quasi-linear in double logarithmic coordinates. Although the attenuation of the overpressure peak in the  $0^\circ$  direction is faster than that in the  $90^\circ$  and  $180^\circ$  directions, the maximum overpressure peak in the  $0^\circ$  direction is larger than that in the other two directions.

- (3) The earth-covered magazine was severely damaged by the internal explosion. The outer space of the earth-covered magazine is divided into four regions according to the dispersion of soil, namely the front ( $-60^\circ$  to  $60^\circ$ ), the rear ( $135^\circ$  to  $225^\circ$ ), and the sides ( $60^\circ$  to  $135^\circ$ ,  $225^\circ$  to  $300^\circ$ ). The maximum projection distance of the debris in the front wall reaches 82 m, and the debris is distributed within the range of  $\pm 60^\circ$ . The further fragments (40 m or more) were confined to a limited sector within the range of  $\pm 30^\circ$ .
- (4) The numerical simulation results are consistent with the experimental results, which can be used to simulate the pressure distribution and fragment projection of the explosion in the earth-covered magazine. Under the internal explosion, the concrete cracks first appeared at the roof and the ground, and then the damage occurred at the intersection of the walls, and then the damage occurred at each surface. After 1.2 ms, the walls were separated and damaged.
- (5) The launch velocity of concrete fragments on the front wall is the largest, which can reach 25 m/s. The other walls and roof show a law of first increasing and then decreasing under the combined action of shock wave and soil, and the maximum velocity can reach 10 m/s. By combining the debris velocity obtained by numerical simulation, the debris motion equation can well predict the projection distance of debris.

**Author Contributions:** Investigation, data curation, and writing—original draft preparation, G.X.; conceptualization, resources, and writing—review and editing, Y.Q.; investigation and writing—review and editing, H.X.; investigation and data curation, X.L.; data curation and writing—review and editing, C.G. All authors have read and agreed to the published version of the manuscript.

**Funding:** This research work was financially supported by the National Key Research and Development Program of China (Grant No. 2021YFC3100700), the Fundamental Research Funds for the Central Universities (Grant No. 30922010408) and the Excellent Postdoctoral Program of Jiangsu Province (Grant No. 288214).

**Data Availability Statement:** No data are included.

**Conflicts of Interest:** The authors declare that they have no known competing financial interests or personal relationships that could have appeared to influence the work reported in this paper.

## References

1. GB 50089-2018; Safety Standard for Design of Engineering of Civil Explosive Materials. China Planning Press: Beijing, China, 2018.
2. Edri, I.; Savir, Z.; Feldgun, V.; Karinski, Y.S.; Yankelevsky, D.Z. On blast pressure analysis due to a partially confined explosion: I. experimental studies. *Int. J. Prot. Struct.* **2011**, *2*, 1–20. [[CrossRef](#)]
3. Ahirwal, B.; Prasad, R.; Kashyap, S.K.; Banerjee, G. Stress analysis due to internal explosion pressure of designed flameproof enclosure for hazardous area. *Process Saf. Prog.* **2019**, *39*, e12100. [[CrossRef](#)]
4. Zyskowski, A.; Sochet, I.; Mavrot, G.; Bailly, P.; Renard, J. Study of the explosion process in a small scale experiment—Structural loading. *J. Loss Prev. Process Ind.* **2004**, *17*, 291–299. [[CrossRef](#)]
5. Tian, L.; Li, Z. Dynamic response analysis of a building structure subjected to ground shock from a tunnel explosion. *Int. J. Impact Eng.* **2008**, *35*, 1164–1178. [[CrossRef](#)]
6. Liu, X.; Gu, W.; Liu, J.; Xu, J.L.; Hu, Y.; Hang, Y. Dynamic response of cylindrical explosion containment vessels subjected to internal blast loading. *Int. J. Impact Eng.* **2020**, *135*, 103389.1–103389.13. [[CrossRef](#)]
7. Baker, W.E.; Cox, P.A.; Westine, P.S.; Kulesz, J.; Strehlow, R.A. *Explosion Hazards and Evaluation*; Elsevier: Amsterdam, The Netherlands, 1983.
8. Guo, Z.; Song, F.; Liu, F.; He, F. Experiment of closed flat box structure subjected to internal detonation. *J. PLA Univ. Sci. Technol.* **2008**, *9*, 345–350.
9. Ding, Y.; Chen, H.; Shi, Y. Simplified Model of Overpressure Loading Caused by Internal Blast. *Eng. Mech.* **2015**, *32*, 119–125+133.
10. Wu, C.Q.; Lukaszewicz, M.; Schebella, K.; Antanovskii, L. Experimental and numerical investigation of confined explosion in a blast chamber. *J. Loss Prev. Process Ind.* **2013**, *26*, 737–750. [[CrossRef](#)]
11. Hu, Y.; Wu, C.; Matthew, L.; Dragos, J.; Ren, J.; Haskett, M. Characteristics of confined blast loading in unvented structures. *Int. J. Prot. Struct.* **2011**, *2*, 21–44. [[CrossRef](#)]
12. Watanabe, M.; Ohno, T.; Beppu, M.; Hasue, K. An experimental study on the mitigation of peak over pressure and fragments due to internal explosion of earth covered magazines. *Collect. Struct. Eng. Treatises* **2011**, *57*, 1124–1133.
13. Beppu, M.; Ohno, T.; Shiomu, M.; Katayama, M. The effect of thickness of covered soil on the properties of blast wave pressure on site due to inner explosion in an earth covered RC explosives magazine. *J. Struct. Eng.* **2008**, *54*, 1022–1033.

14. DoD. *Structures to Resist the Effects of Accidental Explosions (UFC 3-340-02)*; USA Army Corps of Engineering: Washington, DC, USA, 2008.
15. Smith, P.D.; Mays, G.C.; Rose, T.A.; Teo, K.G.; Roberts, B.J. Small scale models of complex geometry for blast overpressure assessment. *Int. J. Impact Eng.* **1992**, *12*, 345–360. [[CrossRef](#)]
16. Yang, Y.; Li, X.; Wang, X.; Zhang, L.; Zhang, M. Scale similarity model of internal explosion in closed field. *J. Vib. Shock* **2014**, *33*, 128–133+140.
17. Wu, Z.; Zhang, P.; Fan, L.; Liu, Q. Debris characteristics and scattering pattern analysis of reinforced concrete slabs subjected to internal blast loads—a numerical study. *Int. J. Impact Eng.* **2019**, *131*, 1–16. [[CrossRef](#)]
18. Yong, L.; Kai, X. Prediction of debris launch velocity of vented concrete structures under internal blast. *Int. J. Impact Eng.* **2007**, *34*, 1753–1767.
19. Pickerd, V.; Bornstein, H.; McCarthy, P.; Buckland, M. Analysis of the structural response and failure of containers subjected to internal blast loading. *Int. J. Impact Eng.* **2016**, *95*, 40–53. [[CrossRef](#)]
20. Gong, S.; Jin, W.L. Prediction of debris launch velocity of reinforced concrete slab subjected to internal blast loading. *Eng. Mech.* **2009**, *26*, 225–230.
21. Li, Z.; Chen, L.; Fang, Q.; Hao, H.; Zhang, Y.; Chen, W.; Xiang, H.; Bao, Q. Study of autoclaved aerated concrete masonry walls under vented gas explosions. *Eng. Struct.* **2017**, *141*, 444–460. [[CrossRef](#)]
22. Fang, Q.; Liu, J.; Zhang, Y.; Qian, Q. Finite element analysis of failure modes of blast-loaded R/C beams. *Eng. Mech.* **2001**, *18*, 1–8.
23. Xu, K.; Lu, Y. Numerical simulation study of spallation in reinforced concrete plates subjected to blast loading. *Comput. Struct.* **2006**, *84*, 431–438. [[CrossRef](#)]
24. *GB 50154-2009*; Safety Code for Design of Underground and Earth Covered Magazine of Powders and Explosives. China Planning Press: Beijing, China, 2009.
25. Kim, D.; Matsumura, T.; Nakayama, Y. Propagation and attenuation characteristics of blast wave pressure generated from an explosion inside an earth-covered magazine. *Sci. Technol. Energ. Mater.* **2013**, *74*, 100–105.
26. *LS-DYNA Keyword User's Manual*; Version 970; Livermore Software Technology Corporation: Livermore, CA, USA, 2007.
27. Zhao, J.; Feng, H.; Tian, H.; Wei, X. Numerical Analysis of Explosion Process in Soil. *J. Archit. Civ. Eng.* **2011**, *28*, 5.
28. Pula, R.; Khan, F.I.; Veitch, B.; Amyotte, P.R. A Model for Estimating the Probability of Missile Impact: Missiles Originating from Bursting Horizontal Cylindrical Vessels. *Process Saf. Prog.* **2007**, *26*, 129–139. [[CrossRef](#)]
29. Fan, S.C.; Yu, Q.J.; Yang, Y.; Lim, H.S.; Kang, K.W. Study of Debris Throw and Dispersion After Break-up of Reinforced Concrete Structures Under Internal Explosion. In Proceedings of the 34th DoD Explosive Safety Seminar, Portland, OR, USA, 13–15 July 2010.
30. Zhang, X.; Chen, G. Analysis methods of projection velocity and flight trajectory of explosion fragments. *J. South China Univ. Technol.* **2009**, *37*, 105–110.
31. Hauptmanns, U. A procedure for analyzing the flight of missiles from explosions of cylindrical vessels. *J. Loss Prev. Process Ind.* **2001**, *14*, 395–402. [[CrossRef](#)]